Environmental Science Advances

ROYAL SOCIETY OF CHEMISTRY

PAPER

View Article Online
View Journal

Cite this: DOI: 10.1039/d5va00420a

Microkinetic characterization of ROS-driven methane production through quantum and classical simulations

Ronghan Zhang, *[ab] Zexuan Wang, *[ab] Kin Tung Michael Ho, [a] Nigel J. D. Graham, [a] Giin-Yu Amy Tan *[b] and Po-Heng Henry Lee *[a]

Received 15th November 2025
Accepted 8th April 2026

DOI: 10.1039/d5va00420a

rsc.li/esadvances

Methane is ubiquitous in natural and engineered settings, but the mechanisms of reactive oxygen species (ROS)-driven methane production in living organisms remain unclear. Unraveling the interactions and microkinetics among ROS, iron species, and organic methyl groups (MET) is crucial for reducing emissions and optimizing energy recovery. In this study, the quantum Harrow–Hassidim–Lloyd (HHL) algorithm and classical Levenberg–Marquardt (LM) algorithm were employed to: (1) investigate the primary pathway of Fe^{3+} and ascorbic acid (ASC) reactions, (2) determine the kinetic parameters for the reaction between $[Fe^{IV}{=}O]^{2+}$ and MET, and (3) simulate the ROS-driven methane production pathway under specific abiotic conditions. The results revealed that Fe^{3+} and ASC are primarily responsible for the redox reaction, with a kinetic rate constant of 1.83×10^{-4} M^{-1} s^{-1} for the reaction between $[Fe^{IV}{=}O]^{2+}$ and MET, and a ~10% conversion rate of MET to methane. Our study establishes a theoretical framework for ROS-driven methane production. While identifying a feasible pathway for engineered and natural systems, further investigation and validation are needed to quantify its specific contribution in complex environments. Furthermore, this work demonstrates the potential of hybrid quantum-classical simulations for microkinetic analysis.

Environmental significance

Methane is a double-edged molecule—an important renewable energy source yet a potent greenhouse gas. This study elucidates a previously unclear abiotic and biotic mechanism of reactive oxygen species (ROS)-driven methane formation, revealing how cellular redox reactions involving Fe^{3+}, ascorbic acid, and methylated compounds can generate methane even in oxygenated environments. By integrating quantum (Harrow–Hassidim–Lloyd) and classical (Levenberg–Marquardt) microkinetic simulations, we quantify key rate constants and demonstrate that ferryl ion reactions, rather than hydroxyl radicals, dominate ROS-mediated methane production. These insights advance understanding of methane cycling in both engineered and natural systems, offering new directions for optimising micro-aerated anaerobic digestion and predicting methane emissions from oxygen-exposed ecosystems under changing redox and oxygen conditions.

1. Introduction

As global warming intensifies, it is of great significance to develop clean energy that can replace fossil fuel energy.[1] Methane is a renewable, clean energy source, albeit also a potent greenhouse gas. Harnessing methane production and collection for energy purposes presents a promising approach to mitigate greenhouse gas emissions. Methane production through anaerobic digestion (AD) can be enhanced by 10–30% using micro-aeration (2.63–37.5 mL O_2/L_R d, where L_R is the reactor working volume), which improves hydrolysis and generates reactive oxygen species (ROS) (0.27–0.29 mM H_2O_2 per cycle.[2–8] Contrary to popular belief that methane can only be produced under anaerobic conditions, enhanced methane formation has been observed in natural systems in the presence of oxygen, including oxygen-rich wetlands and oceans, where the addition of oxygen increased methane emissions by 4–10 fold.[9,10] The ability to produce methane appears to be deeply rooted in evolution and present in all living organisms. Through coupling oxygen-generated ROS with methane production as part of an organism's innate oxidative stress mechanism, this mitigates ROS-induced oxidative damage. For example, *Bacillus subtilis* and *Escherichia coli* showed a 1.2–3.2 times methane yield increases in the presence of ROS as compared to that of non-ROS condition.[3] Leveraging on these emerging insights can provide new avenues for mitigating emissions and improving renewable energy harvesting.

[a]Department of Civil and Environmental Engineering, Imperial College London, London, SW7 2AZ, UK. E-mail: po-heng.lee@imperial.ac.uk

[b]Department of Architecture and Civil Engineering, City University of Hong Kong, Hong Kong SAR, China. E-mail: rzhang343-c@my.cityu.edu.hk; zexuawang4-c@my.cityu.edu.hk; amytan@cityu.edu.hk

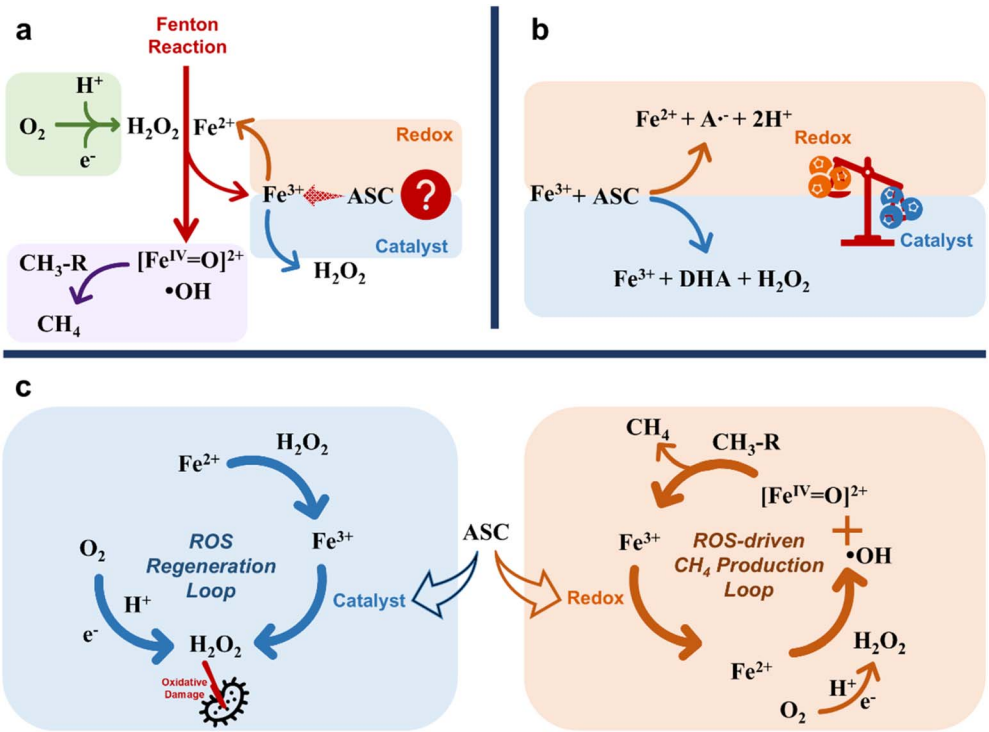

Fig. 1 Proposed reaction pathways of the ROS-driven methane production loop: (a) the chemical processes involved in the biological Fenton reaction; (b) the catalyst and redox reactions between ASC and Fe^{3+}; (c) the two possible reaction loops: ROS regeneration loop and ROS-driven methane production loop.

However, the precise mechanisms and micro-kinetics underlying the role of ROS in facilitating methane production remain poorly understood.

ROS-driven methane production has been linked to the presence of methyl group-containing organosulfur compounds, ROS, $Fe^{2+}$and reducing agent ascorbic acid (ASC) (Fig. 1a).[3,11] Fe^{2+} and H_2O_2 (a form of ROS) can undergo Fenton reaction to generate Fe^{3+}, hydroxyl radicals ($^{\bullet}OH$) and ferryl ions ($[Fe(IV)=O]^{2+}$). $[Fe(IV)=O]^{2+}$ and $^{\bullet}OH$ can react with methyl-containing organosulfur compounds to form methane.[11] The Fe^{3+} produced can be reduced by ASC to regenerate Fe^{2+}, sustaining the Fenton reaction. It is expected that these chemical species are present in natural and AD-engineered systems. Iron, an active metal predominantly coordinated in heme groups and iron-sulfur clusters that drive electron transport chains and participates in redox reactions, is widely present in living organisms including microorganisms.[12] Exposure of microbes to oxygen often produces ROS, which damage cellular structures and impair metabolisms.[13] ASC may play a crucial role in cellular protective mechanisms from ROS damage by facilitating iron and ROS redox reactions, thereby producing methane as a byproduct. However, there is a discrepancy in the proposed mechanisms for the interaction between ASC and iron species (Fig. 1b). Here, two competing mechanisms are possible: a catalytic mechanism proposed by Buettner (eqn (1)) and a redox mechanism proposed by Buettner and Jurkiewicz (eqn (2)),[14,15] as shown below:

$$ASC + Fe^{3+} + O_2 = Fe^{3+} + DHA + H_2O_2 \quad (1)$$

where DHA is dehydroascorbic acid

$$ASC + Fe^{3+} = Fe^{2+} + A^{\bullet -} + 2H^+ \quad (2)$$

where $A^{\bullet -}$ is the ascorbate radical.

Models proposed by Shen *et al.* showed that the catalysis degree of the reaction was 4 to 6-fold greater than that of the redox reaction.[16] However, experimental data from Elmagirbi *et al.* indicated that 76% of Fe^{3+} was converted to Fe^{2+} in the presence of ASC, suggesting that only 24% of Fe^{3+} may participate in the catalyst reaction.[17] Currently, it is unclear which pathway, whether redox or catalysis, plays a more significant role in promoting ROS-activated microkinetics. If the redox reaction between ASC and Fe^{3+} dominates, it can produce Fe^{2+} which promotes the ROS-driven methane production pathway to mitigate oxidative cell damage. In contrast, if the catalytic reaction is dominant, it will produce additional H_2O_2, which can cause cell damage and inhibit the methane production pathway.

Overall, the interaction between ASC and iron species drives two competing loops (Fig. 1c). The catalytic pathway (blue loop) regenerates H_2O_2, potentially leading to ROS accumulation. In contrast, the redox pathway (orange loop) reduces Fe^{3+} to Fe^{2+}, driving the Fenton reaction to generate $[Fe(IV)=O]^{2+}$ and hydroxyl radicals. These intermediates subsequently oxidize methyl-containing organosulfur compounds to produce

methane while regenerating Fe^{3+} for the next cycle. Consequently, determining the dominant microkinetic pathway is essential to distinguish between the ROS regeneration and the methane production loop. Based on this, we hypothesize that methane production proceeds *via* ferryl ions and methyl group-containing organosulfur compounds such as methionine (MET), through the pathway described in eqn (9) (Table 2).

The ROS regeneration loop may produce H_2O_2 continuously and cause cell damage, however, the generation of $^{\bullet}OH$ and $[Fe(IV)=O]^{2+}$ as intermediates in the Fenton-driven methane production loop may contribute to methane production. Addressing the counteracting effects of the ROS regeneration loop and the Fenton-driven methane production loop would require the preferred reaction for ROS-driven methane production microkinetics to be established. To this end, microkinetic simulation was used to determine which reaction cycle (the orange, or blue), or both reaction cycles shown in Fig. 1c is more favorable.

Microkinetic simulation can be conducted using both quantum and classical computing algorithms, each offering its own set of advantages. Most recently, the Harrow Hassidim and Lloyd (HHL) quantum algorithm has been successfully applied in solving linear microkinetic matrices.[18,19] The Levenberg–Marquardt (LM) classical algorithm has already been used to determine the microkinetic parameters with nonlinear matrices.[20–22] These studies have demonstrated the versatility of microkinetic simulation and its potential to couple both quantum and classical computing approaches.

In the context of ROS-driven methane production microkinetics, the mass balance of the reaction between ASC and Fe^{3+} can be formulated as a system of linear equations, whereas that of the associated reactions between ferryl ion and MET can be modelled non-linearly. This study, thus, aims to achieve three objectives: (1) determine the microkinetic model between ASC and Fe^{3+} using the quantum HHL algorithm, (2) employ the classical LM algorithm to calculate the microkinetics between ferryl ion and MET, and (3) simulate the ROS-driven methane-forming microkinetics using the HHL algorithm. The quantum HHL simulation results were benchmarked against classical computations, with further validation conducted against existing experimental data from relevant studies. Additionally, the microkinetics of ROS scavenging, ASC, oxygen, and iron species for ROS-driven methane production will be discussed. The findings of this study will advance our understanding of ROS-driven methane production in natural and engineered systems. Moreover, the insights for future research studies associated with applying quantum and classical computing simulations in microkinetic models are addressed.

2. Methodology

2.1 Simulation parameters and assumptions

To develop our microkinetic simulation, we utilized experimental data from Althoff *et al.*, who investigated abiotic methane formation from organosulfur compounds (MET) in the presence of iron, ascorbate, and H_2O_2.[11,23] We adopted their reported reactant concentrations and environmental conditions to define the initial settings for our computational model (Table 1).

Table 1 Reactants and reaction conditions used in the analysis[11,23]

Reactant	Concentration (mmol L^{-1})
ASC	50
Ferric ion	40
MET	0.5
Hydrogen peroxide	100
Dissolved oxygen	160
Condition	**Value**
pH value	3
Temperature	25 °C
Reaction time	30 h
Reaction volume	1 mL

In this simulation, a pH of 3 was selected for the following reasons: (1) previous research indicated a maximum ROS-driven methane production at pH = 3 based on experiments conducted in the pH range of 1–9.[11] (2) In our case, ROS-driven methane production in *E. coli* likely occurs in the *E. coli* periplasmic cell envelope, where its pH is in the range of pH = 1–3.[24] Since such a pathway is applicable to all organisms, it is plausible to have it in the *E. coli* periplasm.[3] Moreover, ASC formation by *E. coli* has been reported previously, indicating its capability to survive in acidic conditions.[25] Furthermore, *E. coli*, possesses regulatory hydrogenase that can effectively ensure its survival under lower pH conditions (pH ≥ 2).[26] (3) Some archaeal species can still be active even at pH = 1–2.[27] (4) The cytoplasmic proteins of acetogens remain stable under extremely acidic conditions.[28] Therefore, ROS-driven methane production pathways may occur in organisms at low pH.

Table 2 provides a summary of the stoichiometry, reaction kinetics, and thermodynamic constants used for the microkinetic simulations. Here, eqn (1)–(7) were used to describe the interactions between different reactants. The chemical reactions eqn (1)–(4) represent the catalytic and redox reactions between ASC and Fe^{3+}, as well as the interactions between the corresponding products. Eqn (5) and (6) reflect the products of the two Fenton reactions, namely $^{\bullet}OH$ and $[Fe(IV)=O]^{2+}$. Finally, eqn (7) reflects the role of ASC in scavenging $^{\bullet}OH$.

To establish the microkinetic model, several assumptions were made: (1) the molar concentration of DHA in eqn (1) and (4) shown in Table 2 was taken to be the same as the concentration of $HO_2^{\bullet-}$ and H_2O_2, according to the stoichiometric ratio of 1 : 1; (2) the concentration of DHA has a linear relationship with Fe^{3+};[29] (3) the concentration of $O_2^{\bullet-}$ is 3.9 mM, using a conversion rate of 1.5% for $[O_2]$ to $[O_2^{\bullet-}]$ according to previous literature;[30] (4) eqn (2) and (3) can be combined as eqn (8) in Table 2, and since eqn (3) is the rate limiting reaction, the kinetic reaction rate constant can be taken as k_3, (5) the interaction pathway between $[Fe^{IV}=O]^{2+}$ and MET, as proposed by Althoff *et al.*, can be summarized as eqn (9) in Table 2.[11] (6) Reactions eqn (5) and (7) can be

Table 2 Reactions used in this analysis and their standard Gibbs free energies and reaction rate constants at 25 °C[e]

	Reaction	Kinetic parameter (k) (M^{-1} s^{-1})	Reference	Gibbs free energy (ΔG_0) (kcal mol^{-1})	Reference
(1)	$ASC + Fe^{3+} + O_2 = DHA + Fe^{3+} + H_2O_2$	$k_1 = 4.0 \times 10^5$	31	$\Delta G_{0-1} = -10.2$	32 and 33 [a]
(2)	$ASC + Fe^{3+} = Fe^{2+} + 2H^+ + A^{\cdot-}$	$k_2 = 4.5 \times 10^3$	34	$\Delta G_{0-2} = 1.1$	35
(3)	$Fe^{2+} + O_2 = Fe^{3+} + O_2^{\cdot-}$	$k_3 = 1.0 \times 10^{-5}$	36	$\Delta G_{0-3} = -91.6$	37
(4)	$A^{\cdot-} + O_2^{\cdot-} + H_2O = DHA + HO_2^{\cdot-} + OH^-$	$k_4 = 2.6 \times 10^8$	38	$\Delta G_{0-4} = 38.4$	39
(5)	$Fe^{2+} + H_2O_2 = Fe^{3+} + {}^{\cdot}OH + OH^-$	$k_5 = 5.7 \times 10^2$	40	$\Delta G_5 = 28.7$	[b]
(6)	$Fe^{2+} + H_2O_2 = [Fe^{IV}{=}O]^{2+} + H_2O$	$k_6 = 1.0 \times 10^6$	41	$\Delta G_6 = -14.9$	[c]
(7)	$ASC + {}^{\cdot}OH = A^{\cdot-} + H_2O + H^+$	$k_7 = 7.9 \times 10^9$	16	$\Delta G_7 = -30.4$	[b]
(8)	$ASC + O_2 = 2H^+ + O_2^{\cdot-} + A^{\cdot-}$	—	[d]	—	[d]
(9)	$2[Fe^{IV}{=}O]^{2+} + MET + H_2O_2 + 2H^+ = 2Fe^{3+} + HCyA + CH_4 + H_2O$	—	[d]	—	[d]
(10)	$ASC + Fe^{2+} + H_2O_2 = Fe^{3+} + A^{\cdot-} + 2H_2O$	—	[d]	—	[d]

[a] The ΔG_{0-1} was calculated using the relationship $\Delta G_0 = -nF\,E_{cell}$, where $n = 2$ and F is the Faraday constant. E_{cell} is the change of total reaction reduction potential, which was obtained between $E_{(O_2/H_2O_2)} = +0.28V$ and $E_{(dehydroascorbate/ascorbate)} = +0.06V$.[32,33] [b] The ΔG value was calculated based on the standard Gibbs free energies of formation ΔG_f for the individual chemical species.[35,42,43] [c] Calculated using the equilibrium constant (K) estimated from the MATLAB kinetic simulation. [d] Refer to Section 2.1 and SI Table 1. [e] Enzymatic scavengers (SOD, Catalase) are excluded in this study. Their presence *in vivo* regulates ROS levels but does not alter the fundamental role of Ferryl iron in driving methane formation.

combined as eqn (10) in Table 2, and the kinetic reaction rate constant can be taken as k_5 (rate limiting).

2.2 Kinetic estimation using HHL algorithm

In this study, the HHL algorithm was used to simulate microkinetic models to determine the mechanism behind ASC, Fe^{3+}, and the ROS-driven methane production (redox and/or catalysis pathway). We constructed the model according to the chemical equilibrium principle that the rates of forward reaction and reverse reaction are equivalent. The forward reaction rate constant (k) and Gibbs free energy (ΔG_0) used are shown in Table 2 and in the SI Table 1. Detailed calculations are shown in the SI Note 1.

To investigate the mechanism for ROS-driven methane production microkinetics in non-methanogenic microbes at the conditions listed in Table 1, the following system of linear equations was built.

$$A \cdot x = b \tag{11}$$

where A and b are known matrices while x is the unknown matrix to be determined.

The HHL algorithm requires matrix A to be Hermitian, necessitating the transformation of A into matrix A^H.

$$A^H = \begin{bmatrix} 0 & A \\ A^\dagger & 0 \end{bmatrix} \tag{12}$$

where $A^\dagger$ denotes the complex conjugate transpose of A.

After the conversion of matrix (A) of eqn (11) into the Hermitian matrix (A^H) in eqn (12), the unknown term x was calculated using eqn (13) in the HHL algorithm:

$$x = b \times A^{H-1} \tag{13}$$

Hence, to investigate whether the redox and/or catalysis pathway drives the reaction between ASC and Fe^{3+}, a microkinetic linear matrix model (eqn (14)) was constructed based on eqn (1), (4) and (8) at steady state. The procedure for establishing eqn (14) is shown in the SI Note 2.

$$\begin{bmatrix} \frac{1}{50\times10^{-3}} & \frac{1}{50\times10^{-3}} & \frac{1}{50\times10^{-3}} & \frac{1}{50\times10^{-3}} \\ k_1 & 0 & -k_{-1}[DHA] & 0 \\ 0 & -k_{-4}[OH^-][DHA] & 0 & k_4[O_2^{\cdot-}] \\ k_3 & 0 & 0 & -k_{-3}[H^+]^2[O_2^{\cdot-}] \end{bmatrix} \times \begin{bmatrix} ASC \\ HO_2^{\cdot-} \\ H_2O_2 \\ A^{\cdot-} \end{bmatrix} = \begin{bmatrix} 1 \\ 0 \\ 0 \\ 0 \end{bmatrix} \tag{14}$$

To investigate the ROS-driven methane production pathway, a microkinetic linear matrix (eqn (15)) was built initially to simulate the probability of the Fenton reaction forming $[Fe^{(IV)}{=}O]^{2+}$ to participate in the ROS-driven methane production pathway. Eqn (15) was constructed based on reactions eqn (2), (6) and (10) at steady state. The process for establishing eqn (15) is given in the SI Note 3.

$$\begin{bmatrix} \frac{1}{40\times10^{-3}} & \frac{1}{40\times10^{-3}} & \frac{1}{40\times10^{-3}} & 0 \\ k_2[\mathrm{ASC}] & -k_{-2}[\mathrm{H^+}]^2[\mathrm{A^{\bullet -}}] & 0 & 1 \\ -k_{-5}[\mathrm{A^{\bullet -}}] & k_5[\mathrm{ASC}][\mathrm{H_2O_2}] & 0 & 1 \\ 0 & k_6[\mathrm{H_2O_2}] & -k_{-6} & 0 \end{bmatrix} \times \begin{bmatrix} \mathrm{Fe^{3+}} \\ \mathrm{Fe^{2+}} \\ \mathrm{Fe^{IV}}aO^{2+} \\ c \end{bmatrix} = \begin{bmatrix} 1 \\ 0 \\ 0 \\ 0 \end{bmatrix} \quad (15)$$

To investigate the methane production of MET oxidated $[Fe^{(IV)}{=}O]^{2+}$ in the ROS-driven methane production pathway, a microkinetic linear matrix model (eqn (16)) was constructed based on the eqn (9) reaction at steady state. According to the stoichiometric ratio in the eqn (9) reaction, the production of HCyA represents methane production. The process for establishing eqn (16) is shown in the SI Note 3.

$$\begin{bmatrix} \frac{1}{0.5\times10^{-3}} & \frac{1}{0.5\times10^{-3}} \\ k_9\left[\mathrm{Fe^{IV}}aO^{2+}\right]^2[\mathrm{H_2O_2}][\mathrm{H^+}]^2 & -k_{-9}\left[\mathrm{Fe^{3+}}\right]^2 \end{bmatrix} \times \begin{bmatrix} \mathrm{MET} \\ \mathrm{HCyA} \end{bmatrix} = \begin{bmatrix} 1 \\ 0 \end{bmatrix} \quad (16)$$

2.3 Kinetic estimation using LM algorithm

The reaction rate constant between MET and $[Fe^{(IV)}{=}O]^{2+}$ was determined using mass balances derived from reaction eqn (2), (5), (6), (7) and (9). The resulting non-linear matrix (eqn (17)) was solved using MATLAB with a LM algorithm. Further information about the matrix development is given in SI Note 4.
where V denotes the reaction volume, and t refers to the reaction time.

$$\begin{bmatrix} N_{\mathrm{Fe^{2+},Final}} \\ N_{\mathrm{H_2O_2,Final}} \\ N_{\mathrm{Fe^{3+},Final}} \\ N_{\mathrm{\cdot OH,Final}} \\ N_{\mathrm{CH_4,Final}} \\ N_{\mathrm{ASC,Final}} \\ N_{\mathrm{Fe^{IV}O^{2+},Final}} \\ N_{\mathrm{MET,Final}} \end{bmatrix} - \begin{bmatrix} -k_5-k_6 & k_2 & 0 & 0 \\ -k_5-k_6 & 0 & 0 & 0 \\ k_5 & 0 & 0 & 0 \\ k_5 & k_2 & -k_7 & 0 \\ 0 & 0 & 0 & k_9 \\ 0 & -k_2 & -k_7 & 0 \\ 0 & 0 & 0 & -k_9 \\ 0 & 0 & 0 & -k_9 \end{bmatrix} \cdot \begin{matrix} \left[\mathrm{Fe^{2+}}\right]\cdot[\mathrm{H_2O_2}] \\ \left[\mathrm{Fe^{3+}}\right]\cdot[\mathrm{ASC}] \\ \left[\mathrm{Fe^{3+}}\right]\cdot[\mathrm{^{\bullet}OH}] \\ \left[\mathrm{Fe^{IV}}aO^{2+}\right]^2[\mathrm{MET}][\mathrm{H_2O_2}][\mathrm{H^+}]^2 \end{matrix} \cdot V \cdot t - \begin{bmatrix} N_{\mathrm{Fe^{2+},Initial}} \\ N_{\mathrm{H_2O_2,Initial}} \\ N_{\mathrm{Fe^{3+},Initial}} \\ N_{\mathrm{\cdot OH,Initial}} \\ N_{\mathrm{CH_4,Initial}} \\ N_{\mathrm{ASC,Initial}} \\ N_{\mathrm{Fe^{IV}O^{2+},Initial}} \\ N_{\mathrm{MET,Initial}} \end{bmatrix} = 0 \quad (17)$$

3. Results

3.1 Mechanistic determination analysis

Table 3 summarizes the simulated concentrations of the reaction products, $[HO_2^{\bullet -}]$, $[A^{\bullet -}]$ and $[H_2O_2]$ associated with ASC and Fe^{3+} participation in redox and catalytic reactions, respectively. The results obtained using the quantum HHL algorithm showed good agreement with the classical MATLAB simulation. Notably, regarding the catalytic product $[HO_2^{\bullet -}]$, the classical simulation yielded a value of $\sim10^{-20}$ mol L^{-1}. It is important to clarify that this non-zero value represents a numerical artifact (asymptotic residue) inherent to classical ODE solvers using floating-point arithmetic, rather than a physical concentration. In contrast, the quantum simulation reported a concentration of 0.00 mol L^{-1}, correctly identifying the absence of this species within the algorithmic resolution.

Consequently, both simulations confirmed that nearly 100% of the reaction proceeded *via* the redox pathway. This result was consistent with the fact that the Gibbs free energy for eqn (8) ($\Delta G = -90.5$ kcal mol^{-1}) is significantly more negative than that for eqn (1) ($\Delta G = -10.2$ kcal mol^{-1}), indicating a strong thermodynamic preference for the redox pathway. In the presence of oxygen, ASC, and Fe^{3+}, $A^{\bullet -}$ generation by eqn (8) is more favorable. Eqn (8) is dependent on the redox reaction between ASC and Fe^{3+} occurring, rather

Table 3 Summary of the simulation results[a]

Unknown parameter	Estimated values (quantum)	Estimated values (classical)	Remarks	Error
Mechanistic determination by Google Quantum AI & Classical MATLAB				
[ASC]	0.00 (mol L^{-1})	0.00 (mol L^{-1})	—	1.56×10^{-20}
$[HO_2^{\cdot -}]$	0.00 (mol L^{-1})	1.56×10^{-20} (mol L^{-1})	Redox reaction[b]	
$[H_2O_2]$	0.00 (mol L^{-1})	0.00 (mol L^{-1})	Catalytic reaction[b]	
$[A^{\cdot -}]$	5.00×10^{-2} (mol L^{-1})	5.00×10^{-2} (mol L^{-1})	Redox reaction[b]	
Kinetic reaction rate constant determination by Classical MATLAB				
k_9[c]	—	1.83×10^{-4} (M^{-1} s^{-1})	—	—
Microkinetic simulation by Google Quantum AI & Classical MATLAB				
$[Fe^{3+}]$	0.00 (mol L^{-1})	2.93×10^{-7} (mol L^{-1})	0[d]	4.14×10^{-7}
$[Fe^{2+}]$	0.00 (mol L^{-1})	1.20×10^{-11} (mol L^{-1})	0[d]	
$[Fe^{IV}{=}O^{2+}]$	4.00×10^{-2} (mol L^{-1})	4.00×10^{-2} (mol L^{-1})	100%[d]	
[MET]	4.71×10^{-4} (mol L^{-1})	4.71×10^{-4} (mol L^{-1})	—	1.23×10^{-12}
$N_{Methane}$[e]	4.71×10^{-8} mol	4.71×10^{-8} mol	—	
Conversion rate[f]	9.42%		This work	—
Conversion rate[g]	10.00%		Althoff *et al.*[11]	—

[a] Classical results include a numerical artifact from ODE solvers. The residual values ($\sim 10^{-7}$) for trace species are negligible in representing physical concentrations. [b] Products of catalytic/redox reaction indicated in eqn (14). [c] k_9 is the kinetic parameter for eqn (11). [d] The proportion of iron ions involved in Fenton reaction. [e] Methane production. [f] Simulated conversion rate (η) of MET to methane in Google Quantum AI. [g] Experimentally measured conversion rate (η) of MET to methane conducted by Althoff *et al.*[11]

than the catalytic reaction. These findings aligned well with the results of the studies conducted by Timoshnikov *et al.* and Buettner & Jurkiewicz, which showed the high degree of Fe^{3+} reduction by ASC under aerobic conditions and at a pH of 3.[15,44] The simulation results showed that ASC is beneficial for promoting methane production in the Fenton-driven methane production loop. Thus, the redox reaction between ASC and Fe^{3+} plays a decisive role in tilting the microkinetics towards the ROS-driven methane production pathway.

3.2 Kinetic reaction rate constant determination

The kinetic rate constant k_9 in the matrix (eqn (17)) was derived as 1.83×10^{-4} M^{-1} s^{-1} (Table 3) by implementing the LM algorithm in MATLAB. Comparing the reactions represented by eqn (6) and (9), the reaction rate constant (k_9) between $[Fe^{(IV)}{=}O]^{2+}$ and MET is approximately ten orders of magnitude lower than the reaction rate constant (k_6) of the Fenton reaction to produce $[Fe^{(IV)}{=}O]^{2+}$, implying that the reaction of $[Fe^{(IV)}{=}O]^{2+}$ and MET is the rate-determining step in the ROS-driven methane production pathway. SI Table 2 provides a summary of the MATLAB output results.

3.3 Microkinetic simulation

The results derived from the execution of eqn (15) matrix on Google Quantum AI platform were consistent with classical MATLAB computations (Table 3). It is evident that through the Fenton reaction, iron is prone towards ferryl ion formation (4.00×10^{-2} (mol L^{-1}), with near 100% conversion rate from iron to ferryl ion. This result matched the findings of Deguillaume *et al.*, which showed that at a low pH of 3.5, the concentration of ferryl ion produced by the reaction of Fe^{2+} and H_2O_2 was 10^4 times greater than the concentration of $^{\cdot}OH$ produced.[45] From the microkinetics perspective, the kinetic reaction rate constant between Fe^{3+} and H_2O_2 to produce ferryl ion (k_6) is 10^4 times greater than that of $^{\cdot}OH$ formation (k_5) in the ROS-driven methane production process. Fe^{3+} (k_2) and $^{\cdot}OH$ (k_7) exhibit a greater susceptibility to reduction by ASC as compared to k_5. As a result, the ferryl ion serves as a primary reactant with MET to produce methane.

According to the stoichiometric ratio in eqn (9), the product concentration of HCyA is directly proportional to the methane produced. Therefore, methane production can be estimated using eqn (16) through the HHL algorithm. In addition, the conversion rate (η) of MET to methane can be calculated. The quantum-simulated conversion rate (η) was 9.42% (Table 3), showing strong agreement with the classical calculation (10.00%) and the experimental value reported by Althoff *et al.*[11] The detailed calculations are shown in SI Note 5.

4. Discussion

4.1 Effect of radical kinetics and oxygen levels for methane production

An investigation of the $^{\cdot}OH$ concentration in cells is of paramount importance. In the ROS-driven methane production pathway studied in this work (conditions presented in Table 1), $^{\cdot}OH$ produced by the Fenton reaction (Fig. 1c), can either react with methyl compounds to form methane or be scavenged by ASC. ASC reportedly has a strong affinity for $^{\cdot}OH$ with a high reaction rate of 7×10^9 M^{-1} s^{-1}.[46] Meanwhile, the reaction rate constant of $^{\cdot}OH$ attacking intracellular DNA is 3×10^8 M^{-1} s^{-1}.[47] This difference in the order of magnitude indicates that the scavenging effect of ASC occurs at a higher rate than $^{\cdot}OH$-induced cellular damage. As a result, it is proposed that ROS in the methane production pathway does not cause significant damage to cells. Furthermore, the reaction rate constant of

methyl-containing compounds and $^{\bullet}OH$ is 1.5×10^7 M^{-1} s^{-1}, which is notably lower than the scavenging rate of $^{\bullet}OH$ by ASC (7×10^9 M^{-1} s^{-1}).[48] Therefore, the contribution of $^{\bullet}OH$ may not be as significant as that of ferryl ions in the ROS-driven methane production pathway (Fig. 2).

Our findings mechanistically demonstrate the feasibility of a ROS-driven methane production pathway under the specific abiotic conditions modeled. This pathway offers a theoretical framework to interpret methane enhancement phenomena not only in micro-aeration anaerobic digestion (MAAD), but also in natural systems, such as wetlands.[6,49] While these systems can synthesize H_2O_2 under oxygen (~21 μM in wetlands *vs.* 270–290μM in MAAD), which reacts with Fe^{2+} to promote the generation of ferryl ions and facilitates the conversion of MET to methane.[8,50,51] Extrapolating these microkinetic results to complex environmental matrices introduces inherent uncertainties. Factors such as pH variations, organic ligand complexation, and microbial interactions in natural ecosystems may significantly alter the reaction kinetics compared to our simplified model. Recent studies suggest that ROS can promote Fenton reaction in bacteria and archaea, generating ferryl ions that oxidize methyl-containing donors.[3] These biological observations align with our mechanistic findings; however, distinguishing the specific contribution of this ROS-driven pathway from canonical enzymatic processes in diverse oxygen environments requires further *in situ* validation to bridge the gap between idealized modeling and ecosystem complexity.

However, excessively high oxygen levels may negatively impact the overall methane production in these systems. For instance, in cyanobacteria, the conversion rate of organic MET is affected when the oxygen concentration is close to that of air-saturated water.[23,50] Higher intracellular oxygen levels have been shown to lower the conversion rates for both MET (about 10%) and $[Fe^{IV}=O]^{2+}$.[11] In addition, Althoff *et al.* reported a lack of CH_4 formation in an oxygen-saturated environment, most likely due to oxygen's adverse effects on ROS-driven methane production.[23] This might be attributed to the reaction between the methyl radical ($^{\bullet}CH_3$), the methane precursor, and O_2, forming methylperoxyl ($CH_3OO^{\bullet}$) with a significantly high reaction rate constant of 3.7×10^9 M^{-1} s^{-1}.[51] The formation of methylperoxyl reduces the production of methane. This rate constant for the reaction between $^{\bullet}CH_3$ and O_2 is notably larger than the calculated rate constant for the methane production reaction of $[Fe^{IV}=O]^{2+}$ with MET (1.83×10^{-4} M^{-1} s^{-1}) investigated in this study. Aside from ROS-driven methane production, oxygen overload also affects methanogenesis by creating an unfavorable environment for methanogens' survival, lowering the overall methane production rate.[2] Hence, ascertaining the oxygen concentration threshold required for striking a balance between ROS-induced and methanogen-based methane production would be advantageous for engineered systems such as MAAD seeking enhanced methane production as well as the control and mitigation of methane emission from natural ecosystems. Future work must bridge the gap between this idealized microkinetic model and *in situ* environmental conditions to validate these broader implications.

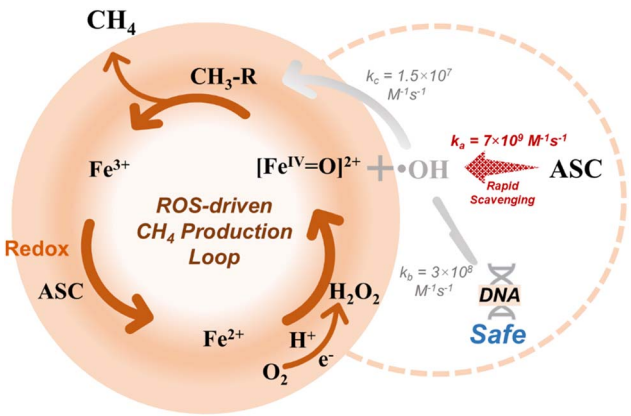

Fig. 2 Schematic indicating that $^{\bullet}OH$ (the product of the Fenton reaction) does not participate in the ROS-driven CH_4 production loop and damages intracellular DNA. k_a is the reaction rate constant between ASC and $^{\bullet}OH$;[46] k_b is the reaction rate constant between DNA and $^{\bullet}OH$;[47] k_c is the reaction rate constant between methyl-containing compounds and $^{\bullet}OH$.[48]

4.2 Perspectives and limitations of microkinetic using quantum computing

Quantum computing incorporates the superposition and entanglement properties of quantum mechanics and can surpasses classical computation in analyzing and quantifying information under certain conditions. Notably, it can efficiently simulate the energy consumption of the Haber–Bosch process (1–2% of global energy consumption), an energy-intensive process, by analyzing the underlying chemical reaction mechanisms.[52] Specifically, the HHL algorithm enables the implementation of chemical microkinetic models on quantum computers, for processes such as CO oxidation, aiding in the resolution of chemical kinetics-related issues.[19,53] Furthermore, Becerra *et al.* used the same quantum algorithm to quantify the uncertainties in Rh(III)-catalyzed CO oxidation pathways, which classical computation struggles to calculate. This emerging trend suggests that quantum computing may be a promising technique for simulating chemical reaction mechanisms and microkinetic models.[18,54] It foreshadows the potential mainstream adoption of quantum simulation for predicting molecular properties, activation energies, and reaction rate constants.[55,56]

While classical solvers remain efficient for these small-scale systems, this study establishes a prospective algorithmic advantage. By replacing classical polynomial scaling (*e.g.*, $O(N^3)$ for matrix inversion), the HHL algorithm offers an exponential speedup with logarithmic scaling ($O(\log N)$).[57] To illustrate this, for a hypothetical large-scale network with $N = 10^6$ species, classical computational cost would surge to 10^{18} operations, whereas the quantum complexity grows only to the order of $\log(10^6)$ (approx. 20). Nevertheless, this scaling analysis indicates that quantum solvers will be indispensable for future large-scale biochemical reaction network simulations, where high dimensionality renders classical approaches computationally prohibitive. This capability will enable the study of more complex environments for further investigation and related systems in the future.

Variations in the oxygen content of organisms may have an impact on ROS concentration, thereby influencing variations in the methane content.[9] Consequently, this study investigated the impact of oxygen concentration in the range of 0–1000 mM in the models. The concentration of $O_2^{\cdot-}$ in the initial model is influenced by the oxygen content, consequently affecting the relative importance of the redox and catalysis reactions. However, the results have shown that the redox reaction dominated within this oxygen concentration range, as detailed in SI Fig. 1. For the microkinetic simulation of ROS-induced methane production modelling, alterations in oxygen concentration ought to influence H_2O_2. However, the model's foundation is based on the chemical experimental data presented by Althoff *et al.*[11,23] Hence, the H_2O_2 concentration remained constant throughout this study. Furthermore, the proportional relationship between the conversion of oxygen to H_2O_2 within living organisms remains unclear and it is not known how much oxygen can be converted into H_2O_2 within a cell. A comprehensive investigation into the influence of oxygen concentration on methane production in methanogenic pathways driven by ROS is thus unattainable. Moreover, the simulation of this work was largely based on the experimental data of Althoff *et al.*, obtained through the reactions of pure chemicals at pH 3.[11] There is a lack of research on ROS-driven methane production in organisms at higher biological pH. In nature and environmental systems such as anaerobic digesters, which operate at circumneutral pH (6.5–8.0), iron speciation differs significantly, often involving precipitation or complexation with organic ligands.[58] These structural changes alter reaction energy barriers and kinetic rate constants (k). To extend our algorithmic framework to these conditions, we propose a hybrid computational strategy: theoretical methods like Density Functional Theory (DFT) or the Variational Quantum Eigensolver (VQE) can be employed to calculate the specific activation energies and rate constants for iron-ligand complexes at neutral pH.[59,60] Additionally, experimental techniques such as Electron Paramagnetic Resonance (EPR) spectroscopy could be integrated in future studies to directly detect the transient ferryl iron intermediates predicted by our model.[61] These derived parameters can then serve as updated inputs for the HHL solver, ensuring the model's applicability across diverse biochemical settings.

From a biological perspective, fermentative bacteria, which are known for their ability to survive and function well in a wide pH range (4–8), could serve as better candidates to study this phenomenon.[62] The intracellular pH is generally lower than the extracellular pH, reaching 3.5 to 4.5.[63] Methods to study methane production *in vivo* such as microbial electromethanogenesis, may be used to explore ROS-driven methane production at pH 3.5 to 7.5 in future investigations.[64]

5. Conclusion

This study employed a hybrid quantum-classical computational framework to investigate the microkinetics of ROS-driven methane production. The results indicate that the redox reaction between ASC and Fe^{3+} is favored over the catalytic pathway, thereby supporting continued Fenton-driven methane production through Fe^{2+} regeneration. The reaction between $[Fe(IV)=O]^{2+}$ and MET was identified as the rate-determining step, and the quantum simulated MET to methane conversion rate showed good agreement with current experimental observations, supporting the proposed mechanistic pathway.

These findings identify a feasible abiotic pathway for ROS-driven methane production and provide a theoretical framework for interpreting methane enhancement phenomena in micro-aeration anaerobic digestion and potentially in natural systems such as wetlands. More broadly, this work demonstrates the potential of the HHL quantum algorithm for microkinetic modelling, particularly in larger biochemical reaction networks where classical computation may become challenging. Further experimental validation under more complex biological conditions will be important for extending the applicability of this framework.

Author contributions

Ronghan Zhang and Zexuan Wang: conceptualization, methodology, software, formal analysis, investigation, writing – original draft, writing – review & editing. Kin Tung Michael Ho: conceptualization, writing – review & editing. Nigel J. D. Graham: writing – review & editing. Giin-Yu Amy Tan: writing – review & editing. Po-Heng Lee: supervision, conceptualization, writing – review & editing.

Conflicts of interest

The authors declare no competing financial interest.

Data availability

The source code and the detailed model-building procedure are available in the supplementary information (SI). Supplementary information is available. See DOI: https://doi.org/10.1039/d5va00420a.

Acknowledgements

The authors gratefully acknowledge Prof. Aleksandra Szczuka from the Department of Civil and Environmental Engineering, University of Michigan, Ann Habour, for her valuable input in modelling and reviewing the paper.

References

1 S. Biswas, A. P. Kulkarni, S. Giddey and S. Bhattacharya, A review on synthesis of methane as a pathway for renewable energy storage with a focus on solid oxide electrolytic cell-based processes, *Front. Energy Res.*, 2020, **8**, 570112.
2 N. Yu, B. Guo, Y. Zhang, L. Zhang, Y. Zhou and Y. Liu, Different micro-aeration rates facilitate production of different end-products from source-diverted blackwater, *Water Res.*, 2020, **177**, 115783.

3 L. Ernst, B. Steinfeld, U. Barayeu, T. Klintzsch, M. Kurth, D. Grimm, T. P. Dick, J. G. Rebelein, I. B. Bischofs and F. Keppler, Methane formation driven by reactive oxygen species across all living organisms, *Nature*, 2022, **603**, 482–487.
4 S. Montalvo, F. Ojeda, C. Huiliñir, L. Guerrero, R. Borja and A. Castillo, Performance evaluation of micro-aerobic hydrolysis of mixed sludge: Optimum aeration and effect on its biochemical methane potential, *J. Environ. Sci. Health Part A*, 2016, **51**, 1269–1277.
5 S.-F. Fu, F. Wang, X.-S. Shi and R.-B. Guo, Impacts of microaeration on the anaerobic digestion of corn straw and the microbial community structure, *Chem. Eng. J.*, 2016, **287**, 523–528.
6 D. Nguyen and S. K. Khanal, A little breath of fresh air into an anaerobic system: How microaeration facilitates anaerobic digestion process, *Biotechnol. Adv.*, 2018, **36**, 1971–1983.
7 Q. Chen, W. Wu, D. Qi, Y. Ding and Z. Zhao, Review on microaeration-based anaerobic digestion: State of the art, challenges, and prospectives, *Sci. Total Environ.*, 2020, **710**, 136388.
8 X. Liu, D. Huang, C. Zhu, F. Zhu, X. Zhu and D. Zhou, Production of reactive oxygen species during redox manipulation and its potential impacts on activated sludge wastewater treatment processes, *Environ. Sci. Technol.*, 2024, **58**, 23042–23052.
9 J. C. Angle, T. H. Morin, L. M. Solden, A. B. Narrowe, G. J. Smith, M. A. Borton, C. Rey-Sanchez, R. A. Daly, G. Mirfenderesgi and D. W. Hoyt, Methanogenesis in oxygenated soils is a substantial fraction of wetland methane emissions, *Nat. Commun.*, 2017, **8**, 1567.
10 A. V. Borges, W. Champenois, N. Gypens, B. Delille and J. Harlay, Massive marine methane emissions from near-shore shallow coastal areas, *Sci. Rep.*, 2016, **6**, 27908.
11 F. Althoff, K. Benzing, P. Comba, C. McRoberts, D. R. Boyd, S. Greiner and F. Keppler, Abiotic methanogenesis from organosulphur compounds under ambient conditions, *Nat. Commun.*, 2014, **5**, 4205.
12 E. R. Frawley and F. C. Fang, The ins and outs of bacterial iron metabolism, *Mol. Microbiol.*, 2014, **93**, 609–616.
13 F. Keppler, L. Ernst, D. Polag, J. Zhang and M. Boros, ROS-driven cellular methane formation: Potential implications for health sciences, *Clin. Transl. Med.*, 2022, **12**(7), e905.
14 G. R. Buettner, In the absence of catalytic metals ascorbate does not autoxidize at pH 7: ascorbate as a test for catalytic metals, *J. Biochem. Biophys. Methods*, 1988, **16**, 27–40.
15 G. R. Buettner and B. A. Jurkiewicz, Catalytic metals, ascorbate and free radicals: combinations to avoid, *Radiat. Res.*, 1996, **145**, 532–541.
16 J. Shen, P. T. Griffiths, S. J. Campbell, B. Utinger, M. Kalberer and S. E. Paulson, Ascorbate oxidation by iron, copper and reactive oxygen species: Review, model development, and derivation of key rate constants, *Sci. Rep.*, 2021, **11**, 7417.
17 A. Elmagirbi, H. Sulistyarti and A. Atikah, Study of ascorbic acid as iron (III) reducing agent for spectrophotometric iron speciation, *J. Pure Appl. Chem. Res.*, 2012, **1**, 11–17.
18 A. Becerra, A. Prabhu, M. S. Rongali, S. C. S. Velpur, B. Debusschere and E. A. Walker, How a quantum computer could quantify uncertainty in microkinetic models, *J. Phys. Chem. Lett.*, 2021, **12**, 6955–6960.
19 E. A. Walker and S. A. Pallathadka, How a quantum computer could solve a microkinetic model, *J. Phys. Chem. Lett.*, 2020, **12**, 592–597.
20 H. P. Gavin, *The Levenberg-Marquardt algorithm for nonlinear least squares curve-fitting problems*, Department of Civil and Environmental Engineering Duke University, 2019, vol. 3, pp. 1–23.
21 K. Toch, J. Thybaut, B. Vandegehuchte, C. Narasimhan, L. Domokos and G. Marin, A Single-Event MicroKinetic model for "ethylbenzene dealkylation/xylene isomerization" on Pt/H-ZSM-5 zeolite catalyst, *Appl. Catal., A*, 2012, **425**, 130–144.
22 F. Jin, Y. Fan, M. Yuan, F. Min, G. Wu, Y. Ding and G. F. Froment, Single-event kinetic modeling of ethene oligomerization on ZSM-5, *Catal. Today*, 2018, **316**, 129–141.
23 F. Althoff, A. Jugold and F. Keppler, Methane formation by oxidation of ascorbic acid using iron minerals and hydrogen peroxide, *Chemosphere*, 2010, **80**, 286–292.
24 D. He, M. Zhang, S. Liu, X. Xie and P. R. Chen, Protease-mediated protein quality control for bacterial acid resistance, *Cell Chem. Biol.*, 2019, **26**, 144–150.
25 Z. Zhang, M. Aboulwafa, M. H. Smith and M. H. Saier Jr, The ascorbate transporter of Escherichia coli, *J. Bacteriol.*, 2003, **185**, 2243–2250.
26 K. Noguchi, D. P. Riggins, K. C. Eldahan, R. D. Kitko and J. L. Slonczewski, Hydrogenase-3 contributes to anaerobic acid resistance of Escherichia coli, *PLoS One*, 2010, **5**, e10132.
27 C. Baker-Austin and M. Dopson, Life in acid: pH homeostasis in acidophiles, *Trends Microbiol.*, 2007, **15**, 165–171.
28 J. A. Francois and T. J. Kappock, Alanine racemase from the acidophile Acetobacter aceti, *Protein Expr. Purif.*, 2007, **51**, 39–48.
29 S. J. Campbell, B. Utinger, D. M. Lienhard, S. E. Paulson, J. Shen, P. T. Griffiths, A. C. Stell and M. Kalberer, Development of a physiologically relevant online chemical assay to quantify aerosol oxidative potential, *Anal. Chem.*, 2019, **91**, 13088–13095.
30 S. W. Schaffer and M. S. Suleiman, *Mitochondria: the Dynamic Organelle*, Springer Science & Business Media, 2010.
31 M. T. Khan and A. E. Martell, Metal ion and metal chelate catalyzed oxidation of ascorbic acid by molecular oxygen. I. Cupric and ferric ion catalyzed oxidation, *J. Am. Chem. Soc.*, 1967, **89**, 4176–4185.
32 P. M. Wood, The potential diagram for oxygen at pH 7, *Biochem. J.*, 1988, **253**, 287.
33 I. H. Segel, *Biochemical Calculations: How to Solve Mathematical Problems in General Biochemistry*, John Wiley & Sons, 1991.
34 H. Sun, G. Xie, D. He and L. Zhang, Ascorbic acid promoted magnetite Fenton degradation of alachlor: Mechanistic insights and kinetic modeling, *Appl. Catal. B Environ.*, 2020, **267**, 118383.
35 D. H. Truong, T. C. Ngo, N. T. A. Nhung, D. T. Quang, T. L. A. Nguyen, D. Khiri, S. Taamalli, F. Louis, A. El Bakali

and D. Q. Dao, New insights into the competition between antioxidant activities and pro-oxidant risks of rosmarinic acid, *RSC Adv.*, 2022, **12**, 1499–1514.

36 W. Stumm and J. J. Morgan, *Aquatic Chemistry: Chemical Equilibria and Rates in Natural Waters*, John Wiley & Sons, 2013.

37 C. A. Juan, J. M. Pérez de la Lastra, F. J. Plou and E. Pérez-Lebeña, The chemistry of reactive oxygen species (ROS) revisited: outlining their role in biological macromolecules (DNA, lipids and proteins) and induced pathologies, *Int. J. Mol. Sci.*, 2021, **22**, 4642.

38 W. Bors and G. Buettner, *The Vitamin C Radical and its Reactions*, 1997.

39 Y.-J. Tu, D. Njus and H. B. Schlegel, A theoretical study of ascorbic acid oxidation and HOO/O 2- radical scavenging, *Org. Biomol. Chem.*, 2017, **15**, 4417–4431.

40 Z. Wang, J. Jiang, S. Pang, Y. Zhou, C. Guan, Y. Gao, J. Li, Y. Yang, W. Qiu and C. Jiang, Is sulfate radical really generated from peroxydisulfate activated by iron (II) for environmental decontamination?, *Environ. Sci. Technol.*, 2018, **52**, 11276–11284.

41 G. Tachiev, J. Roth and A. Bowers, Kinetics of hydrogen peroxide decomposition with complexed and "free" iron catalysts, *Int. J. Chem. Kinet.*, 2000, **32**, 24–35.

42 P. Refait, C. Bon, L. Simon, G. Bourrie, F. Trolard, J. Bessière and J.-M. Génin, Chemical composition and Gibbs standard free energy of formation of Fe (II)-Fe (III) hydroxysulphate green rust and Fe (II) hydroxide, *Clay Miner.*, 1999, **34**, 499–510.

43 N. Bazhin, Standard and transformed values of gibbs energy formation for some radicals and ions involved in biochemical reactions, *Arch. Biochem. Biophys.*, 2020, **686**, 108282.

44 V. A. Timoshnikov, T. V. Kobzeva, N. E. Polyakov and G. J. Kontoghiorghes, Redox interactions of vitamin C and iron: Inhibition of the pro-oxidant activity by deferiprone, *Int. J. Mol. Sci.*, 2020, **21**, 3967.

45 L. Deguillaume, M. Leriche and N. Chaumerliac, Impact of radical versus non-radical pathway in the Fenton chemistry on the iron redox cycle in clouds, *Chemosphere*, 2005, **60**, 718–724.

46 B. HALLIWELL, Ascorbic acid and the illuminated chloroplast, in *Ascorbic Acid: Chemistry, Metabolism, and Uses*, ACS Publications, 1982.

47 M. A. SIDDIQI and E. BOTHE, Single- and double-strand break formation in DNA irradiated in aqueous solution: dependence on dose and OH radical scavenger concentration, *Radiat. Res.*, 1987, **112**, 449–463.

48 R. Herscu-Kluska, A. Masarwa, M. Saphier, H. Cohen and D. Meyerstein, Mechanism of the reaction of radicals with peroxides and dimethyl sulfoxide in aqueous solution, *Chem.–Eur. J.*, 2008, **14**, 5880–5889.

49 J. L. Wilmoth, J. K. Schaefer, D. R. Schlesinger, S. W. Roth, P. G. Hatcher, J. K. Shoemaker and X. Zhang, The role of oxygen in stimulating methane production in wetlands, *Glob. Change Biol.*, 2021, **27**, 5831–5847.

50 S. Kihara, D. A. Hartzler and S. Savikhin, Oxygen concentration inside a functioning photosynthetic cell, *Biophys. J.*, 2014, **106**, 1882–1889.

51 A. Sauer, H. Cohen and D. Meyerstein, The methyl (cyclam) nickel (III) dication in aqueous solutions: determination of the equilibrium constant of homolysis, kinetics of oxygen insertion, and methyl transfer to aquated chromium (2+), *Inorg. Chem.*, 1988, **27**, 4578–4581.

52 C. Tang and S.-Z. Qiao, How to explore ambient electrocatalytic nitrogen reduction reliably and insightfully, *Chem. Soc. Rev.*, 2019, **48**, 3166–3180.

53 S. Matera, W. F. Schneider, A. Heyden and A. Savara, Progress in accurate chemical kinetic modeling, simulations, and parameter estimation for heterogeneous catalysis, *ACS Catal.*, 2019, **9**, 6624–6647.

54 S. Sharma, Quantum algorithms for simulation of quantum chemistry problems by quantum computers: an appraisal, *Found. Chem.*, 2022, **24**, 263–276.

55 M. Reiher, N. Wiebe, K. M. Svore, D. Wecker and M. Troyer, *Elucidating Reaction Mechanisms on Quantum Computers*, Proceedings of the national academy of sciences, 2017, vol. 114, pp. 7555–7560.

56 J. D. Whitfield, J. Biamonte and A. Aspuru-Guzik, Simulation of electronic structure Hamiltonians using quantum computers, *Mol. Phys.*, 2011, **109**, 735–750.

57 A. W. Harrow, A. Hassidim and S. Lloyd, Quantum algorithm for linear systems of equations, *Phys. Rev. Lett.*, 2009, **103**, 150502.

58 V. V. Nenonen, R. Kaegi, S. J. Hug, J. Luster, J. Göttlicher, S. Mangold, L. H. Winkel and A. Voegelin, Effects of organic ligands, phosphate and Ca on the structure and composition of Fe (III)-precipitates formed by Fe (II) oxidation at near-neutral pH, *Environ. Sci.: Processes Impacts*, 2025, **27**, 2479–2506.

59 U. Azad and H. Singh, Quantum chemistry calculations using energy derivatives on quantum computers, *Chem. Phys.*, 2022, **558**, 111506.

60 S.-C. Liu, X.-R. Zhu, D.-Y. Liu and D.-C. Fang, DFT calculations in solution systems: solvation energy, dispersion energy and entropy, *Phys. Chem. Chem. Phys.*, 2023, **25**, 913–931.

61 J. Krzystek, J. England, K. Ray, A. Ozarowski, D. Smirnov, L. Que Jr and J. Telser, Determination by high-frequency and-field EPR of zero-field splitting in iron (IV) oxo complexes: Implications for intermediates in nonheme iron enzymes, *Inorg. Chem.*, 2008, **47**, 3483–3485.

62 B. F. Staley, F. L. de los Reyes III and M. A. Barlaz, Effect of spatial differences in microbial activity, pH, and substrate levels on methanogenesis initiation in refuse, *Appl. Environ. Microbiol.*, 2011, **77**, 2381–2391.

63 M. Flinck, S. Kramer and S. Pedersen, Roles of pH in control of cell proliferation, *Acta Physiol.*, 2018, **223**, e13068.

64 G. Pelaz, D. Carrillo-Pena, A. Morán and A. Escapa, Microbial electromethanogenesis for energy storage: Influence of acidic pH on process performance, *J. Energy Storage*, 2024, **75**, 109685.

